INTERNATIONAL JOURNAL FOR NUMERICAL METHODS IN ENGINEERING
Int. J. Numer. Meth. Engng 2017; **00**:1–35
Published online in Wiley Online Library (www.onlinelibrary.wiley.com). DOI: 10.1002/nme.5606

Accepted Article

Imposition of essential boundary conditions in the material point method

M. Cortis*[1], W. M. Coombs[1], C.E. Augarde[1], M.J.Z. Brown[2], A. Brennan[2], S. Robinson[2]

[1] *School of Engineering and Computing Sciences, Durham University, Durham, UK*
[2] *Civil Engineering, University of Dundee, Fulton Building, Dundee, DD1 4HN, UK*

SUMMARY

There is increasing interest in the Material Point Method (MPM) as a means of modelling solid mechanics problems in which very large deformations occur, e.g. in the study of landslides and metal forming, however some aspects vital to wider use of the method have to date been ignored, in particular methods for imposing essential boundary conditions in the case where the problem domain boundary does not coincide with the background grid element edges. In this paper we develop a simple procedure originally devised for standard finite elements for the imposition of essential boundary conditions, to the MPM, expanding its capabilities to boundaries of any inclination. To the authors' knowledge this is the first time that a method has been proposed that allows arbitrary Dirichlet boundary conditions (zero and non-zero values at any inclination) to be imposed in the MPM. The method presented in this paper is different from other MPM boundary approximation approaches, in that: (i) the boundaries are independent of the background mesh, (ii) artificially stiff regions of material points are avoided and (iii) the method does not rely on spurious *mirroring* of the problem domain to imposed symmetry. The main contribution of this work is equally applicable to standard finite elements and the MPM. Copyright © 2017 John Wiley & Sons, Ltd.

Received . . .

KEY WORDS: material point method, embedded boundaries, non-matching meshes

*Correspondence to: michael.cortis@durham.ac.uk, School of Engineering and Computing Sciences, Durham University, Durham, UK

This article has been accepted for publication and undergone full peer review but has not been through the copyediting, typesetting, pagination and proofreading process, which may lead to differences between this version and the Version of Record. Please cite this article as doi: 10.1002/nme.5606

This article is protected by copyright. All rights reserved.

Accepted Article

1. INTRODUCTION

In recent years, a large number of alternatives to standard finite element (FE) methods have been proposed for the solution of engineering problems in solid mechanics, particularly those involving very large deformations, a challenge to any Lagrangian mesh-based method due to mesh distortion, and the computational expense of remeshing during a simulation. Meshless methods, such as the Element-free Galerkin method [1] and others covered in recent reviews e.g. [2, 3] remain computationally uncompetitive, while other options that are suggested have other disadvantages, e.g. Remeshing and Interpolation Technique with Small Strain (RITSS) [4] which is itself still mesh-based, the Discrete Element Method (DEM) [5] (computationally expensive for real-world geometries) or Smoothed Particle Hydrodynamics (SPH) [6] which has difficulties with solid material modelling.

An exciting alternative to the options discussed above is the material point method (MPM). This is, to date, an underexploited method for which the first description was given in explicit form in the mid-1990s [7] with an implicit version, close to the conventional FE method, appearing in 2003 [8]. In the MPM, discretisation occurs via meshless material points within the problem domain, which are enclosed in a separate mesh (denoted the "grid" from here for clarity) of conventional FEs. The MPM stores information at the material points. These carry information from step to step of an analysis, but the calculations (for equilibrium or momentum balance) are carried out on the (usually regular) surrounding grid with input data obtained via interpolation from the points. The grid is discarded at the end of each load increment or time step and a new grid used at the next step, totally avoiding the mesh distortion problem found with FEs. One advantage of the MPM over other meshless methods is in computational efficiency as the governing equations are assembled and solved on a regular background grid without the need for neighbour searches or basis function determination. The MPM is often compared to Arbitrary Lagrangian-Eulerian (ALE) finite element formulations (e.g. see [9]), however ALE methods differ from MPMs in an important respect, that is, they need mapping of state variables when updating meshes and MPM does not, all information being carried at the material points. The original MPM is usually presented as an explicit approach which models a problem domain by lumping volumes or masses at material points. Later developments have sought to improve performance by introducing zones of influence around each material point via the use of basis functions with local support (the Generalised Interpolation Material Point (GIMP) approach in [10]). This serves to smooth out the changes in stiffness as material points move between grid elements. More recently, techniques have been developed which track the changes to the volumes linked to material points via local deformation gradient measures [11, 12]). The MPM and its more advanced variants have been applied to many problems

This article is protected by copyright. All rights reserved.

Accepted Article

particularly in geotechnics (e.g. 2D slope stability [13,14] and 2D two-phase dynamic analysis [15]), fracture [16], impact [17] and biomechanics [18].

A key feature of the MPM is the lack of any link between the background grid of elements on which calculation takes place and the material points which represent the problem domain, and a key challenge is how to impose boundary conditions, which are required on the former but defined on the latter. Similar issues arise in the use of meshless methods [19,20] and authors resort to using penalty, Lagrange multiplier or Nitsche methods to impose Dirichlet boundary conditions (see [19] for a comprehensive review on the application of boundary conditions in meshless methods). However, it should be noted at this point that here we are not concerned with a lack of Kronecker delta property as seen with Moving Least Squares (MLS)-based meshless methods [3]. A key advantage of the MPM is its use of shape functions based on standard FEs for the actual solution.

We consider that the issue of imposing essential boundary conditions in the MPM has not to date been adequately addressed in the literature and the purpose of this paper is to introduce a new method accurately to impose essential boundary conditions in an implicit manner in the MPM, an approach developed from a similar idea for standard finite elements [21]. The motivation for the work described below arises from a research project in which the MPM is being developed to model seabed ploughing (required for the installation of cables and pipelines for offshore energy infrastructure) linked to experimental research in the laboratory and the field [22]. In the simulation of a plough share passing through soil, rigid surfaces are required to have non-zero essential boundary conditions, where the surfaces have no parity with coordinate or grid directions. The ability to model boundary conditions that are not coincident with the background mesh in the MPM also opens up the applicability of the method to new areas, namely those involving complex geometry and moving boundary conditions, for example materials processing, debris flow with obstructions, silo flow, amongst others. It also allows the MPM to taken advantage of arbitrarily positioned lines of symmetry in numerical analysis to reduce the computational effort.

The paper is organised as follows. In §2 the background to the MPM is briefly reviewed and an approach for imposing essential boundary conditions implicitly in standard FEs with non-coincident boundaries is outlined. In §3 the extension of the implicit essential boundary condition method to 3D and to inclined boundaries is described in detail and particular issues associated with its use with the MPM are explored. In §4 the numerical implementation for imposition of implicit boundaries in the MPM is discussed. In §5 the new method is validated on a range of simple model problems. §6 completes the paper with suggestions for further avenues of research.

This article is protected by copyright. All rights reserved.

Accepted Article

2. BACKGROUND

2.1. The material point method

The novelty of the material point method is its combination of Lagrangian and Eulerian approaches into a single procedure. Since its first presentation in the 1990s [7] many papers have appeared, both developing the MPM and applying it to various problems, as indicated above. In the majority of papers, the MPM is presented in explicit form, however there are advantages in using an implicit approach [8], for example implicit approaches allow for much larger loadsteps to be applied, have improved stability and contain error control within each loadstep. In particular, [8] demonstrated the advantage of adopting an implicit approach for quasi-static analysis in terms accuracy and we follow an implicit approach in this paper. The focus of this paper is on incorporating (and extending) the implicit boundary method within the material point method we therefore restrict ourselves to infinitesimal strains and isotropic linear elastic material behaviour. It should however be noted that the implicit boundary method presented in this paper does not change if we remove these restrictions. The majority of this section uses index notation to detail the formulation; only the discrete nodal equations are given in matrix-vector form for convenience.

The weak form of equilibrium of a body subject to an admissible displacement field, u_i, when inertia is neglected, can be expressed as

$$\int_{\Omega} \big(\sigma_{ij}(\nabla\eta)_{ij} - b_i\eta_i\big)dv - \int_{\partial\Omega} \big(t_i\eta_i\big)ds = 0, \tag{1}$$

where the domain, Ω, is subject to body forces, b_i, and tractions, t_i, on the boundary of the material domain, $\partial\Omega$, causing a set of admissible virtual displacements through the body, η_i. Within this statement of equilibrium the conventional infinitesimal strain is the fundamental variable that characterises the deformation at a material point

$$\varepsilon_{ij} = \frac{1}{2}\left(\frac{\partial u_i}{\partial x_j} + \frac{\partial u_j}{\partial x_i}\right), \tag{2}$$

where x_i are the coordinates of the material point and u_i are the material point's displacements. In this paper a linear relationship is assumed between engineering strain, ε_{ij}, and the Cauchy stress, σ_{ij}, that is

$$\sigma_{ij} = D^{\mathrm{e}}_{ijkl}\varepsilon_{kl}, \tag{3}$$

where D^{e}_{ijkl} is the conventional linear elastic isotropic material stiffness tensor.

This article is protected by copyright. All rights reserved.

Accepted Article

2.2. *Discrete implementation*

We start by introducing the element approximation for the displacements at a point within a finite element

$$\{u\} = [N]\{d^e\} \qquad \text{and} \qquad \{\eta\} = [N]\{d^e_\eta\}, \tag{4}$$

where $\{d^e\}$ and $\{d^e_\eta\}$ are the physical and virtual element nodal displacements, respectively, and $[N]$ is the shape function matrix. The Galerkin form of the weak statement of equilibrium over an element, E, can be obtained from (1) and (4) as

$$\{f^R_e\} = \int_E [B]^T\{\sigma\}dv - \int_E [N]^T\{b\}dv - \int_{\partial\Omega} [N]^T\{t\}ds = \{0\}, \tag{5}$$

where $[B] = [L][N]$ is the strain-displacement matrix containing the spatial derivatives of the shape functions with respect to the nodal coordinates, $[L]$ is the gradient operator matrix, and the superscript $(\cdot)^R$ denotes a residual. The first term in (5) is the internal force within an element and the combination of the second and third terms is the external force vector. Note that the integration of the traction vector remains over the boundary of the domain as we do not assume that the boundaries of the physical domain and the element edges coincide.

The Galerkin form of the weak statement of equilibrium, (5), can be discretised by material points into the following form

$$\{f^R_e\} = \sum_{p=1}^{n_{mp}} [B]^T\{\sigma^p\}v_p - \sum_{p=1}^{n_{mp}} [N]^T\{b\}v_p - \int_{\partial\Omega} [N]^T\{t\}ds = \{0\}, \tag{6}$$

where the sub or superscript p denotes a quantity associated with a material point, n_{mp} is the number of material points within the element under consideration and v_p is the material point volume. In (6), the material point volume, v_p, replaces the quadrature weights and Jacobian volume mapping seen in conventional finite element methods. The volume of a material point can be specified in a number of ways. If the material points are equally spaced across the physical domain, the overall volume can be split equally between the material points. An alternative is to specify the material points' initial positions within each element based on a Gauss quadrature scheme. The volumes of these points would then be the appropriate Gauss quadrature weights multiplied by the determinant of the Jacobian of the parent element (in the case of a uniform grid this would be a constant factor for all elements). Details of the approach for specifying material point volumes in this work are given in Section 4. In (6), the shape function, $[N]$, and strain-displacement, $[B]$, matrices are determined by evaluating the conventional finite element shape functions (or their derivatives) at the material point position within the element.

This article is protected by copyright. All rights reserved.

Linearising (5) or (6) with respect to the unknown nodal displacements, and assuming that the applied body forces and surface tractions are independent of the nodal displacements, gives the element contribution to the global stiffness matrix as

$$[k^E] = \int_E [B]^T [D^e][B] dv \approx \sum_{p=1}^{n_{mp}} [B]^T [D^e][B] v_p. \tag{7}$$

In material point (MP) methods (7) is evaluated through the summation of the MP stiffness contributions within each element, where the nodal stiffness components of a single MP is given by

$$[k^p] = [B]^T [D^e][B] v_p \tag{8}$$

and a material point's contribution to the internal force vector can be determined from

$$\{f^p\} = [B]^T \{\sigma^p\} v_p. \tag{9}$$

The current stress and strain states at the material point is obtained through

$$\{\sigma_n^p\} = \{\sigma_{n-1}^p\} + [D^e][B]\{\Delta d^e\} \qquad \text{and} \qquad \{\varepsilon_n^p\} = \{\varepsilon_{n-1}^p\} + \underbrace{[B]\{\Delta d^e\}}_{\{\Delta\varepsilon\}}, \tag{10}$$

where $\{\Delta d^e\}$ are the incremental element nodal displacements associated with the nth loadstep, $\{\sigma_{n-1}^p\}$ is the MP stress from the previous loadstep (or the original state on the first loadstep) and $\{\Delta\varepsilon\}$ is the strain increment at the material point associated with the loadstep.

The MPM presented in this paper is an incrementally linear method. Within each loadstep the material behaviour is assumed to be linear and the material point contributions to the internal force vector, (9), are linearly dependent on the nodal displacements. However, the material point positions are updated at the end of each loadstep through

$$\{x_n^p\} = \{x_{n-1}^p\} + [N]\{\Delta d^e\}, \tag{11}$$

where $\{x_{n-1}^p\}$ is the material point position from the previous loadstep and $[N]$ contains the shape functions associated with the material point's parent element. This means that the stiffness contribution of a material point its parent element will change as between each loadstep. Therefore, the global stiffness matrix and the internal force vector must be recalculated at the start of each loadstep.

This article is protected by copyright. All rights reserved.

Accepted Article

Accepted Article

2.3. Algorithmic steps

In this paper we adopt an implicit quasi-static formulation of the MPM and the steps in the implemented algorithm are concisely summarised below.

The applied body forces and/or tractions are split into a number of loadsteps and for each of these steps the following process is adopted:

1. calculate the stiffness contribution, $[k^p]$, of all of the material points using (8) and assemble the individual contribution of each material point into the global stiffness matrix, $[K]$;
2. calculate the internal force contribution, $\{f^p\}$, of all of the material points using (9) and assemble the contributions into the global internal force vector, $\{f^R\}$;
3. increment the external tractions and/or body force in (6) and solve for the nodal displacements in within a loadstep, through
$$\{\Delta d\} = [K]\{f^R\}, \tag{12}$$
where $\{\Delta d\}$ are the nodal displacements within the loadsteps and $\{f^R\}$ is the out of balance force residual between the stresses at the material points and the external tractions/body forces. The material point stresses, $\{\sigma^p\}$, used in (6) are obtained from the end of the previous loadstep;
4. the material point positions and stresses can then be updated through interpolation from the incremental nodal displacements using (11) and (10), respectively;
5. reset or replace the background grid.

Note that in this paper we reset the background grid after each loadstep to the original regular background grid. However, at step 5 the grid can be changed or a completely new grid introduced as required. The implicit MPM described above has recently been extended to include generalized basis functions, the GIMP approach of [10], and full descriptions and validations are given in [23, 24].

2.4. Imposition of essential boundary conditions

Since calculations in the MPM take place using the background grid, it is there that boundary conditions should be applied. Imposition of an essential boundary condition where a displacement component is set to zero, can be achieved by aligning the problem domain boundary with a grid boundary and maintaining that grid boundary in all the grids used. However this is often inconvenient and is not possible for an arbitrary geometry or for where a non-zero essential boundary condition is applied. Figure 1(a) illustrates this using a rigid footing foundation problem, where the footing is modelled by imposing non-zero displacements on a part of the problem domain boundary. Figure 1(b) shows the problem domain discretised with material points, surrounded by a grid of four-noded quadrilateral elements. While one could align the grid to the two sides and

This article is protected by copyright. All rights reserved.

Accepted Article

base of the problem domain to impose zero essential boundaries there, this is impossible for the non-zero essential boundary at the footing. Many demonstrations of the MPM to date have avoided tackling this issue either by modelling problems where the boundaries are aligned to the grid (e.g. most slope stability modelling) or other workarounds (such as introducing stiff regions of material points, for example see [25]). An example can be found in [11] where the zero essential boundary at the end of a cantilever is simulated by adding a whole "ghost" cantilever behind the support, subject to the same loading and with the same discretization, thus ensuring symmetry at the fixed end of the cantilever. This type of workaround can only be applied in special cases and is computationally tiresome, at least doubling the cost of any numerical simulation. It is clearly an impediment to the modelling of more challenging problems, such as a moving plough share in 3D or even just a curved boundary. A recent advance in this area has been the development of a "moving mesh concept" in the MPM, e.g. [26], in which part of the background grid is updated to move with a moving essential boundary condition, however this approach loses one of the advantages of the MPM, that a regular structured grid can be reused without change between load or time steps and it is also incapable of modelling a boundary which changes shape. Although it is possible to model some of the problems in this paper with a MPM based on a triangular background grid (see [27, 28], amongst others), the use of a regular quadrilateral mesh has two important advantages, namely: (i) a regular quadrilateral mesh makes material point-element searches trivial, (ii) some extensions to the MPM, for example the generalised interpolation material point (GIMP) method [10], can only be applied to rectangular background grids.

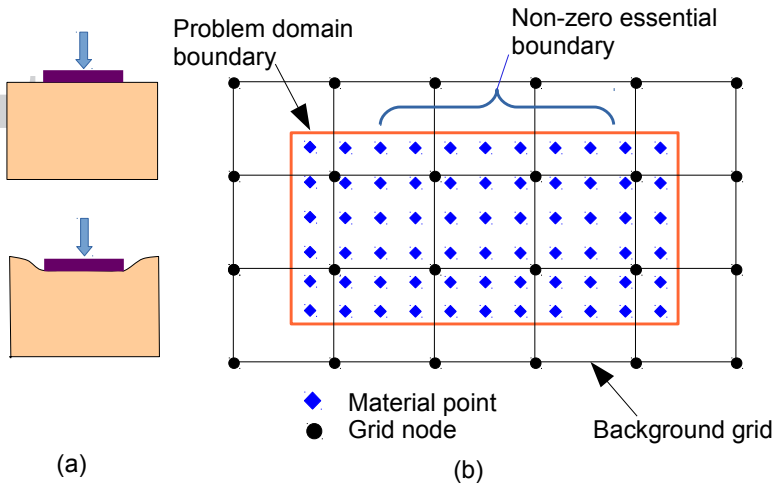

Figure 1. (a) A rigid footing problem. (b) Modelling using the MPM: zero and non-zero essential boundaries.

The issue discussed above for the MPM is linked to the wider problem of imposing constraints on non-matching meshes or the use of so-called "embedded domains", for which there is a growing body of literature, e.g. [29–32] that has links to attempts to impose essential boundary conditions

This article is protected by copyright. All rights reserved.

Accepted Article

in meshless methods (e.g. [19]), i.e. the choice of penalty, Lagrange multiplier or Nitsche methods. Here, however, we take a simpler approach using the work of Kumar and co-workers [21, 33–35] in which the same issue is tackled (in part) for the case of standard finite elements, i.e. a problem domain is discretised with finite elements and essential boundary conditions must be applied on surfaces/edges which are not aligned with element edges. Kumar and co-workers start from an idea originally developed in the 1950s by Kantorovich and Krylov [36] which is also discussed in [29]. The approach in [21, 33–35] is termed an implicit boundary (IB) method and was presented for the case of fixed essential boundaries parallel to one of the coordinate axes for the 2D case. Here we extend the general IB method to allow for fixed, roller and prescribed essential boundary conditions at any inclination with respect to the coordinate axes and then demonstrate its implementation in the MPM framework. The development is given for the 2D case for clarity and to maintain links with [21, 33–35]. The main contribution of this work is equally applicable to standard finite elements and the MPM. The IB approach is conceptually similar to the earlier worth of Höllig and co-workers [37–39] in that they both directly modify interpolation functions to impose the essential boundary conditions [40]. The Weighted Extended B-spline (WEB) method of Höllig uses an R-function [41] to weight the interpolation functions to impose homogeneous Dirichlet boundary conditions. However, a clear distinction between the work of Höllig and co-workers [37–39] and the IB method is that the latter allows inhomogeneous Dirichlet boundary conditions to be imposed independent of the discretisation. The very recent work of Zhang and Zhao [40] provides an extension to the IB method through generalising the boundary value function. They combine these advances with the finite cell method, and the level set method to represent the boundaries, to provide a general method for the imposing of inhomogeneous Dirichlet boundary conditions in two-dimensions for thermo-elasticity. In this paper we adopt the earlier approach of [21, 33–35], extend it to allow boundaries at any inclination, and combine the approach with the MPM to provide, for the first time, a general method to impose inhomogeneous Dirichlet boundary conditions.

At this point it is important to note that other methods also exist which remove the link between a mesh and a problem domain feature, notably the eXtended FEM (XFEM) [42, 43], where the shape functions are enriched to allow the modelling of a displacement discontinuity representing a crack within an element but this is a different problem to the one tackled here.

3. INCLINED IMPLICIT ESSENTIAL BOUNDARY CONDITIONS

In this section we first present the IB method given in [21, 33–35] which applies to boundaries parallel to one of the coordinate axes. We then demonstrate how it can be amended for boundaries at any inclination. The key idea in the IB method is to define trial and test function spaces which

This article is protected by copyright. All rights reserved.

will implicitly lead to the enforcement of the essential boundary conditions, i.e.

$$\{u'\} = [D]\{u\} + \{u^a\} \tag{13}$$

$$\{\eta'\} = [D]\{\eta\}, \tag{14}$$

for the trial and test functions respectively where $[D] = diag(D_1, \ldots, D_{n_d})$ and n_d is the dimensionality. The prime notations $\{u'\}$ and $\{\eta'\}$ have been introduced into equations (13) and (14) to distinguish them from the standard finite element displacement approximation. In Eqn (13), $\{u\}$ is the standard approximation for displacement in a finite element (i.e. as given by Eqn (4)) while $\{u^a\}$ is the essential boundary condition (i.e. zero for a fixed degree of freedom or non-zero for a prescribed displacement). At the implicitly defined boundary, the first term in Eqn (13) will be suppressed via the matrix $[D]$, enforcing the essential boundary condition in the second term. Substituting the trial and test functions into the weak form (Eqn (1)) leads to expressions for the stiffness matrices of elements containing essential boundary conditions (given in detail below).

The implicit essential boundaries are defined by signed distance functions ϕ_j in $\mathcal{R}^2$ for the 2D case, where $\phi_j < 0$ indicates the exterior and $\phi_j > 0$ the interior of the problem domain for the jth boundary. On the boundary $\phi_j = 0$. Essential boundary (or Dirichlet) functions $d_j(\phi_j)$ are then defined for each boundary, which are equal to zero on the boundary and outside the domain, inside the domain it rises to unity at a small distance δ away from the boundary. d_j are often simple C^0 continuous quadratic functions in ϕ_j. At points where more than one essential boundary is active, i.e. at a domain corner, then the product of the $d(\phi_j)$ forms the essential boundary function and in general we write the net essential boundary at a point as

$$D_k = \prod_j d(\phi_j), \tag{15}$$

where k refers to the component of displacement defined at that boundary. D_k are then the components of the diagonal matrix $[D]$ in Eqn (13). Here, following the work of [21], we adopt the following Dirichlet function

$$d = \begin{cases} 0, & \phi < 0 \\ 1 - \left(1 - \frac{\phi}{\delta}\right)^2 & 0 \leq \phi \leq \delta \\ 1 & \phi > \delta \end{cases} \tag{16}$$

where δ is the dimension over which the Dirichlet function d_j (for a boundary condition j) varies from zero to one. A key omission from the original development of this idea, and one of the motivations for the current paper, is the means of modelling "roller" boundary conditions

This article is protected by copyright. All rights reserved.

Accepted Article

(zero displacement in the normal direction combined with zero traction in the tangential direction), however inspection of Eqn (13) reveals this to amount to setting D_k to unity for the coordinate direction that is free. Figure 2 shows the 2D essential boundary matrices for the case of "roller" boundary conditions along two boundaries.

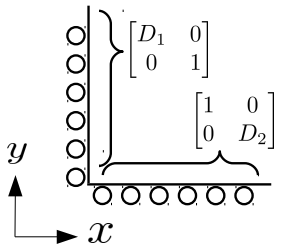

Figure 2. 2D essential boundary matrices for roller boundaries.

3.1. Stiffness matrices

Substituting the trial and test functions into the weak form and following the algorithm given above, leads to the element stiffness matrix in (7) where the effect of the implicit boundary conditions is to alter the form of the $[B]$ matrix [21, 34]. For a bilinear quadrilateral element on the background grid $[B]$ is a $3 \times 2n_{en}$ strain displacement matrix, where n_{en} is the number of nodes per element. The latter is built from blocks for each element node j as

$$[B_j] = \begin{bmatrix} D_1 \frac{\partial N_j}{\partial x} + N_j \frac{\partial D_1}{\partial x} & 0 \\ 0 & D_2 \frac{\partial N_j}{\partial y} + N_j \frac{\partial D_2}{\partial y} \\ D_1 \frac{\partial N_j}{\partial y} + N_j \frac{\partial D_1}{\partial y} & D_2 \frac{\partial N_j}{\partial x} + N_j \frac{\partial D_2}{\partial x} \end{bmatrix}. \tag{17}$$

$[k^E]$ in Eqn (7) can be expanded as follows:

$$[k^E] = \int_{V_e} [B_1]^T [D^e][B_1] dV + \int_{V_e} [B_1]^T [D^e][B_2] dV + \int_{V_e} [B_2]^T [D^e][B_1] dV + \int_{V_e} [B_2]^T [D^e][B_2] dV, \tag{18}$$

or more concisely as

$$[k^E] = [K_1] + ([K_2] + [K_2]^T) + [K_3],$$

where $[K_1]$ is the standard finite element stiffness matrix and in the MPM is obtained through the summation of the MP contributions using (8), and $[K_2]$ and $[K_3]$ contain Dirichlet functions and their derivatives if the element concerned is intersected by an essential boundary. The building

This article is protected by copyright. All rights reserved.

Accepted Article

Accepted Article

blocks for $[K_2]$ and $[K_3]$ are as follows, where j again refers to an element node,

$$[B_{1j}] = \begin{bmatrix} D_1\frac{\partial N_j}{\partial x} & 0 \\ 0 & D_2\frac{\partial N_j}{\partial y} \\ D_1\frac{\partial N_j}{\partial y} & D_2\frac{\partial N_j}{\partial x} \end{bmatrix} = \underbrace{\begin{bmatrix} D_1 & 0 & 0 & 0 \\ 0 & D_2 & 0 & 0 \\ 0 & 0 & D_1 & D_2 \end{bmatrix}}_{[\bar{D}_1]} \underbrace{\begin{bmatrix} \frac{\partial N_j}{\partial x} & 0 \\ 0 & \frac{\partial N_j}{\partial y} \\ \frac{\partial N_j}{\partial y} & 0 \\ 0 & \frac{\partial N_j}{\partial x} \end{bmatrix}}_{[\bar{B}_{1j}]}, \tag{19}$$

or more compactly as

$$[B_{1j}] = [\bar{D}_1][\bar{B}_{1j}]$$

and

$$[B_{2j}] = \begin{bmatrix} N_j\frac{\partial D_1}{\partial x} & 0 \\ 0 & N_j\frac{\partial D_2}{\partial x} \\ N_j\frac{\partial D_1}{\partial y} & N_j\frac{\partial D_2}{\partial x} \end{bmatrix} = \underbrace{\begin{bmatrix} \frac{\partial D_1}{\partial x} & 0 \\ 0 & \frac{\partial D_2}{\partial y} \\ \frac{\partial D_1}{\partial y} & \frac{\partial D_2}{\partial x} \end{bmatrix}}_{[\bar{D}_2]} \underbrace{\begin{bmatrix} N_j & 0 \\ 0 & N_j \end{bmatrix}}_{[\bar{B}_{2j}]} \tag{20}$$

and again this can be compactly expressed as

$$[B_{2j}] = [\bar{D}_2][\bar{B}_{2j}].$$

The calculation of these additional stiffness matrices can be simplified by recognising that along a boundary the Dirichlet functions and their derivatives are constant along a tangential coordinate, and that outside the band of width δ contributions to $[K_2]$ and $[K_3]$ will be zero. If we term the coordinate directions as (n, t) as indicated in Figure 3(a) then we can integrate within the band as

$$[K_2] = \int_{V_e} [B_1]^T [D^e][B_2] dV = \int_t [\bar{B}_1]^T \left(\int_0^\delta [\bar{D}_1]^T [D^e][\bar{D}_2] dn \right) [\bar{B}_2] dt \tag{21}$$

$$[K_3] = \int_{V_e} [B_2]^T [D^e][B_2] dV = \int_t [\bar{B}_2]^T \left(\int_0^\delta [\bar{D}_2]^T [D^e][\bar{D}_2] dn \right) [\bar{B}_2] dt. \tag{22}$$

This article is protected by copyright. All rights reserved.

For the case of a roller boundary permitting translation in the t-direction (e.g. Figure 3(a)) then

$$[\bar{D}_1] = \begin{bmatrix} D_1 & 0 & 0 & 0 \\ 0 & 1 & 0 & 0 \\ 0 & 0 & D_1 & 1 \end{bmatrix} \tag{23}$$

$$[\bar{D}_2] = \begin{bmatrix} \frac{\partial D_1}{\partial x} & 0 \\ 0 & 0 \\ 0 & 0 \end{bmatrix} \tag{24}$$

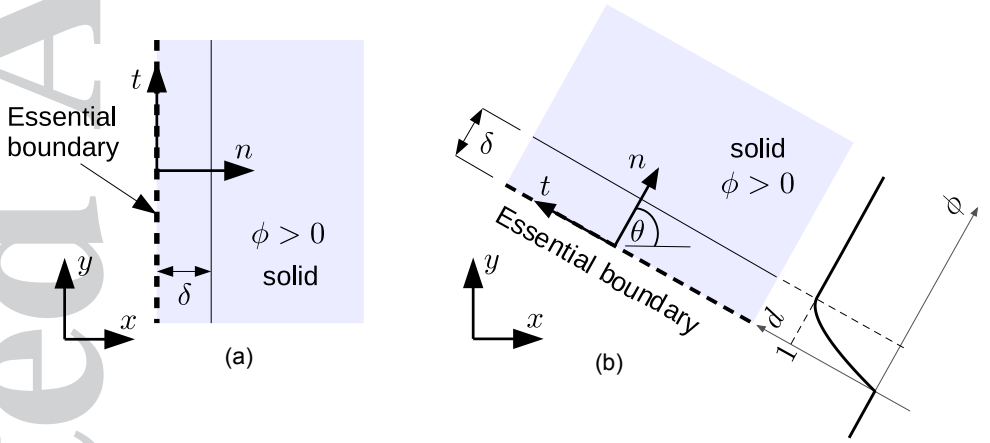

Figure 3. Coordinate system used for integration for stiffness matrix terms: (a) IB parallel to the global coordinate direction; (b) IB inclined to coordinate direction.

3.2. Inclined essential boundaries

In [21, 34], IBs are confined to those parallel to one of the coordinate axes and no guidance is provided on the case of inclined implicit boundaries. In Figure 3(b) the boundary is aligned so that the n-axis is rotated by θ from the x-direction. The variation of the Dirichlet function, d, with distance from the essential boundary is also shown. Note that, as defined by (16), the function varies from zero at the boundary to unity at a distance δ into the solid material. If full fixity was required along this boundary then one would simply define D_1 and D_2 in the x and y directions and use the procedure given above, since full-fixity implies no effect locally of boundary inclination. However, with the motivation mentioned above to develop a model of ploughing, we have determined the amendments necessary to the IB method given above. Matrix $[\bar{D}_1]$ contains values of the Dirichlet function and therefore is invariant with respect to the coordinate system used for its calculation in the band of width δ. However, the components of matrix $[\bar{D}_2]$ are derivatives of the Dirichlet functions with respect to the (x, y) system, and therefore require a transformation if the boundary is

This article is protected by copyright. All rights reserved.

Accepted Article

Accepted Article

inclined. This can be shown to be a simple transformation matrix

$$[T] = \begin{bmatrix} \frac{\partial n}{\partial x} & \frac{\partial n}{\partial y} \\ \frac{\partial t}{\partial x} & \frac{\partial t}{\partial y} \end{bmatrix} = \begin{bmatrix} \cos\theta & \sin\theta \\ -\sin\theta & \cos\theta \end{bmatrix}, \tag{25}$$

so that for any IB, inclined or not

$$[K_2] = \int_t [\bar{B}_1]^T \left(\int_0^\delta [\bar{D}_1]^T [C][\bar{D}_2][T] dn \right) [\bar{B}_2] dt \tag{26}$$

and

$$[K_3] = \int_t [\bar{B}_2]^T \left(\int_0^\delta [T]^T [\bar{D}_2]^T [C][\bar{D}_2][T] dn \right) [\bar{B}_2] dt. \tag{27}$$

It is worth noting that in most cases, components of $[K_2]$ are much smaller than components of $[K_3]$, since the non-derivative terms are much smaller than the derivative terms. It should also be highlighted that the distance function matrix, $[\bar{D}_1]$, does not need to be mapped between coordinate systems as in contains distances, that remain unchanged by a change in coordinate, rather than direction components as in $[\bar{D}_2]$.

4. NUMERICAL IMPLEMENTATION

In this section, the numerical implementation for imposition of implicit boundaries in MPM is discussed. Firstly we discuss the pre-processing stages required to set up a MPM problem, and secondly how local stiffness matrices are evaluated that cover both the material stiffness and the implicit boundaries.

Consider a problem domain (Figure 4(a)) subjected to prescribed, roller and fixed essential boundaries. The domain is discretized into a set of material points, each with an associated volume covered by the material point. A regular background grid of elements on which the governing equation will be solved is then set up (here linear quadrilateral elements are used). Material points are then inserted in every grid element, as shown in Figure 4(b). The material points can conveniently be positioned at standard Gauss quadrature locations and volumes calculated accordingly, but there is no requirement for this. In the next step, all material points with volumes entirely outside the domain are removed, as shown in Figure 4(c). Volumes are adjusted for any material points with volumes partly outside the domain (Figure 4(d)), and the material point position is relocated to the centroid of the remaining solid region (see Figure 4(e)). This process ensures that the total volume (and mass) of the domain is captured by the material points.

This article is protected by copyright. All rights reserved.

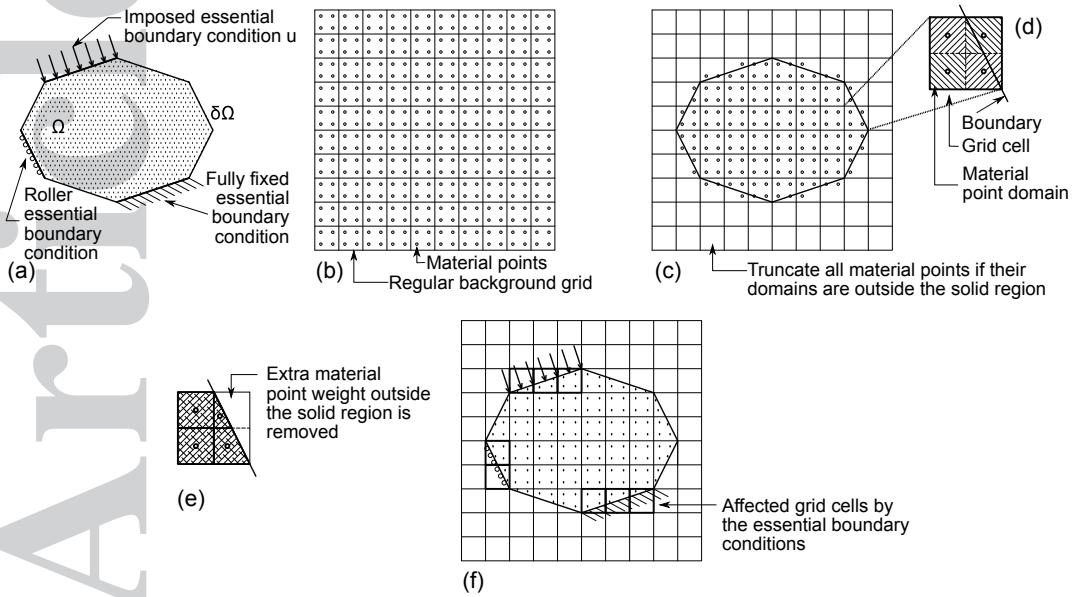

Figure 4. Pre-processing of MPM: (a) the domain and its essential boundaries conditions; (b) MPM background grid and initial set of material points; (c) truncation of material points outside the domain; (d) material point volumes where a boundary passes through a single grid element; (e) resizing of the material point volumes; (f) highlighted grid elements with imposed essential boundary conditions.

After discretizing the domain into the set of material points, the local stiffness matrices $[k^E]$ of every grid element are evaluated using Equation (18). This contains both the material stiffness matrix $[K_1]$ and the implicit penalty stiffness matrices $[K_2]$ and $[K_3]$ that ensure the imposition of any essential boundary conditions on the element (Figure 4(f)). If no essential boundary conditions coincide with the element then $[K_2]$ and $[K_3]$ are zero. To assemble the global stiffness matrix, each element $[k^E]$ is evaluated for elements containing material points and any empty elements are ignored. For elements intersected by essential boundaries, $[K_2]$ and $[K_3]$ are evaluated in a two-stage process. Firstly, the inner integrals of Equations (26) and (27) across the band δ are evaluated using a 3-point Gauss quadrature scheme. Once the inner integrals are evaluated, the outer integrals are evaluated along the boundary segment within the element using a 10-point scheme (see Figure 5). If a non-zero essential boundary condition is required, i.e. $\{u_a\} \neq 0$, the equivalent reaction force to cause this displacement $\{f_R^E\}$ is determined as

$$\{f_R^E\} = [[K_2] + [K_2]^T + [K_3]]\{u_a\} \tag{28}$$

and included in the linear system to be solved.

Equations (26) , (27) and (28) are valid for both curved and straight boundaries and the inner integrals in (26) and (27) are evaluated in the same way in both cases. For curved boundaries the outer integral is approximately by a series of quadrature points within each element where the

This article is protected by copyright. All rights reserved.

Accepted Article

Accepted Article

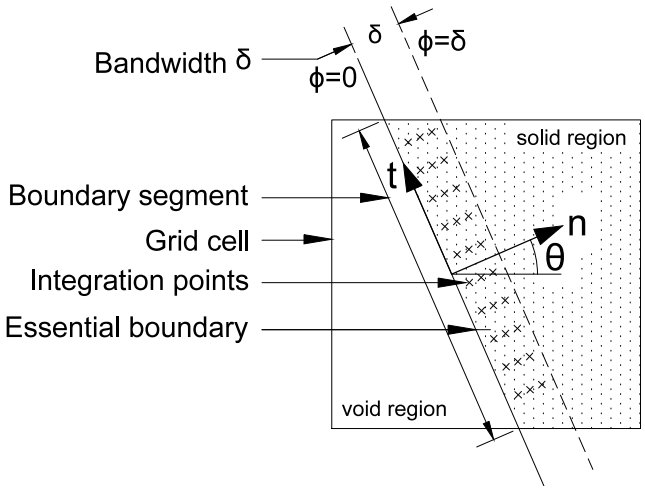

Figure 5. Essential boundary bandwidth δ through grid element

normal and tangential directions will vary along the segment. In this way the implicit boundary method provides a piecewise linear approximation to the edge of the domain.

5. NUMERICAL EXAMPLES

A number of numerical examples are now presented to demonstrate the performance of the implicit essential boundary condition implementation in the MPM described in detail above. All examples are 2D plane strain, use linear elastic material (with Young's modulus of 1000 MPa and Poisson's ratio of 0.3) and an infinitesimal stress-strain relationship, as detailed in §2. The examples presented in this section are designed to validate the implicit boundary conditions and quantify the errors associated with them for relatively simple problems. The performance of the approach is judged using error measures based on analytical solutions which are available for all examples presented, apart from one where comparison is made to a standard finite element solution. The displacement error over the whole domain, r_u, is approximated by the volume-weighted summation of the material point displacement errors, r_u^p

$$r_u = \frac{1}{V}\sum_{p=1}^{n_{mp}} v_p r_u^p, \qquad \text{where} \qquad r_u^p = \frac{||\{u_p\} - \{u_e\}||}{||\{u_e\}||}. \tag{29}$$

$\{u_p\}$ and $\{u_e\}$ are the material point and analytical (or exact) displacement vectors, n_{mp} is the number of material points in the simulation, V is the total volume and $||\{\cdot\}||$ denotes the L2 norm of a vector. The stress error over the domain, $r_{\sigma_{ij}}$, is computed in a similar way from the errors at

This article is protected by copyright. All rights reserved.

each material point, $r^p_{\sigma_{ij}}$, that is

$$r_{\sigma_{ij}} = \frac{1}{V}\sum_{p=1}^{n_{mp}} v_p r^p_{\sigma_{ij}}, \qquad \text{with} \qquad r^p_{\sigma_{ij}} = \frac{|\sigma^p_{ij} - \sigma^e_{ij}|}{|\sigma^e_{ij}|} \tag{30}$$

where σ^p_{ij} and σ^e_{ij} are the material point and analytical stresses. In the sections that follow, (29) and (30) are used to report both the error at a material point and the total error across the domain.

5.1. Compression of a contained block

The first example investigates the ability of inclined roller boundaries, modelled as described above, to deliver accurate results and also examines the effect of the choice of bandwidth δ. The problem is the compression of a 100 mm by 100 mm block of material contained between three roller boundaries, where a prescribed displacement of 1 mm is applied to the fourth boundary in a single loadstep, a problem introduced in [44]. Figure 6 shows the problem at three inclinations, to test the transformation for inclined roller boundaries. In each case the background grid is aligned to the (x, y) axes of the 0° model and single material points are generated in each grid element, as described in §4. The width of the band over which the integrations in (21) and (22) are executed is $\delta = 10^{-6}h$ where h is the grid size (initially set to 10 mm). In this is constant stress problem the stress over the whole domain should be equal to

$$\{\sigma_{xx} \quad \sigma_{yy} \quad \sigma_{xy}\}^T = \{13.46 \qquad 5.77 \qquad 0.00\}^T \quad \text{MPa.}$$

Figures 7a, 8a and 9a show the absolute displacement error over the problem domain, while Figures 7b, 8b and 9b show the absolute stress error in the direction of the applied displacement, σ_{xx}. The maximum displacement error at any point in any of the simulations is 6.09×10^{-6} mm which is good given the relatively small number of material points (one material point per background grid cell). Symmetry is maintained in all of the displacement error distributions and the discontinuous nature of the stress error is due to the low order (bi-linear) element basis and that we do not apply smoothing to the error distributions. Table I gives overall displacement (29) and stress (30) error values for each model. The smallest errors occur in the 0° and 90° models with higher errors seen in the 30° and 45° models, likely indicating integration errors from partially filled elements and truncated material point domains. It should also be noted that the results from the 0° and 90° models are identical, demonstrating the objectivity of the method when integration accuracy variations are removed.

Convergence plots for displacement errors with respect to the bandwidth δ and the degree of refinement are shown in Figures 10, 11 and 12, where h is the size of the background grid elements.

This article is protected by copyright. All rights reserved.

Accepted Article

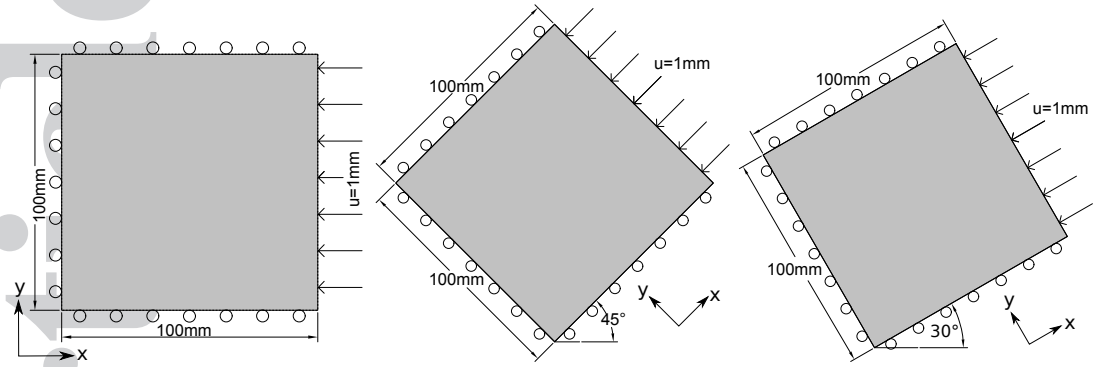

(a) 0° Model (b) 45° Model (c) 30° Model

Figure 6. Compression of a contained block.

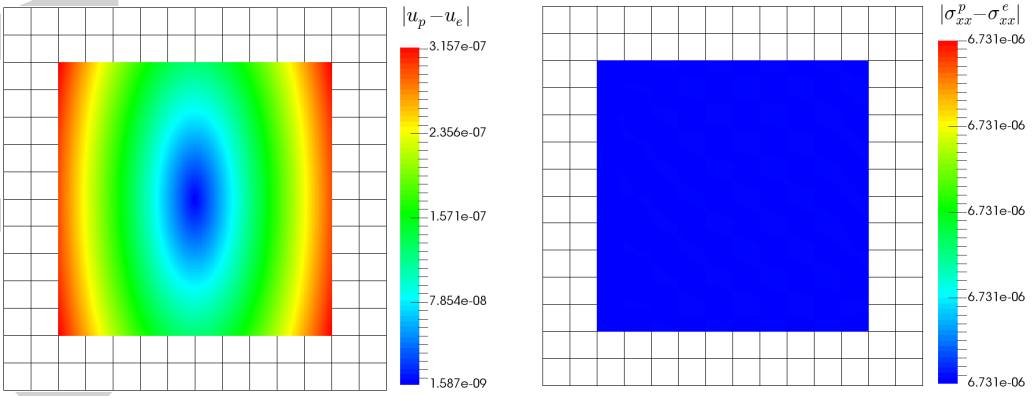

(a) Displacement, $|u_p - u_e|$ (mm) (b) Stress, $|\sigma^p_{xx} - \sigma^e_{xx}|$ (MPa)

Figure 7. Compression of a contained block (0° model): material point errors.

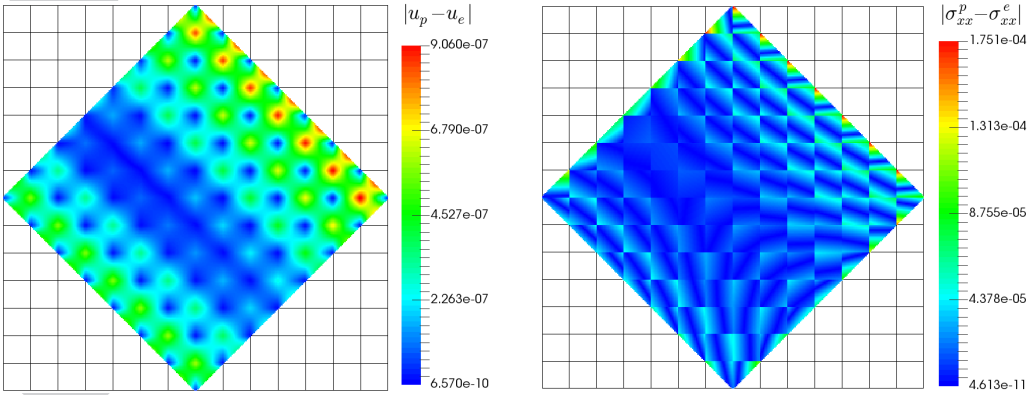

(a) Displacement, $|u_p - u_e|$ (mm) (b) Stress, $|\sigma^p_{xx} - \sigma^e_{xx}|$ (MPa)

Figure 8. Compression of a contained block (45° model): material point errors.

Based on conventional finite element theory the displacement error should converge at a rate of $p+1$, where p is the polynomial order of the finite element basis. In this case, using linear finite elements ($p = 1$), a finite element implementation using the same boundary approximation method

This article is protected by copyright. All rights reserved.

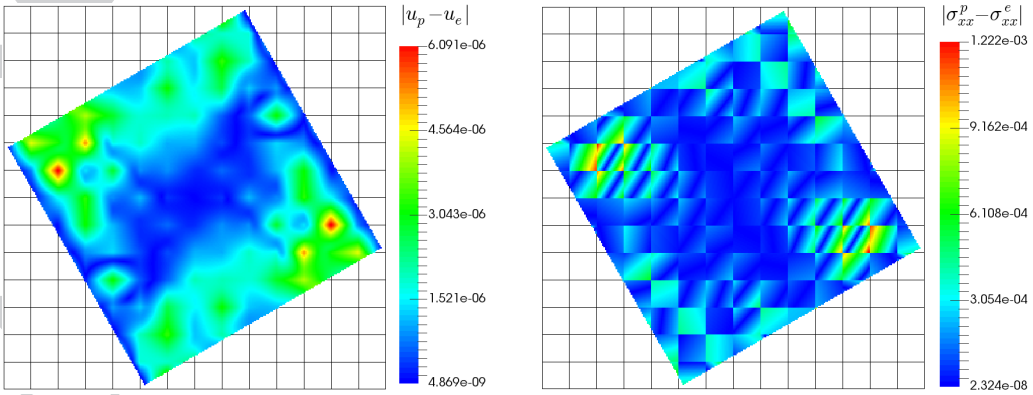

(a) Displacement, $|u_p - u_e|$ (mm) (b) Stress, $|\sigma^p_{xx} - \sigma^e_{xx}|$ (MPa)

Figure 9. Compression of a contained block (30° model): material point errors.

Boundary inclination	r_u	$r_{\sigma_{xx}}$
0° Model	1.573×10^{-9}	5.804×10^{-9}
45° Model	2.036×10^{-9}	9.133×10^{-9}
30° Model	1.173×10^{-8}	1.299×10^{-8}
90° Model	1.573×10^{-9}	5.804×10^{-9}

Table I. Compression of a contained block: domain errors.

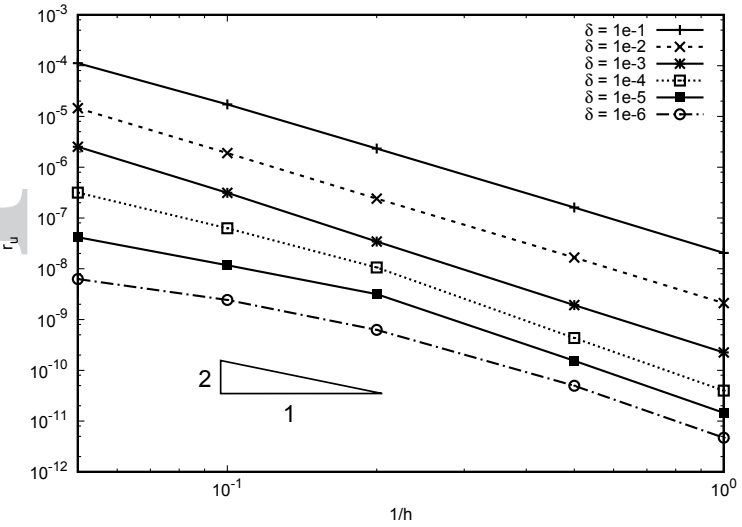

Figure 10. Compression of a contained block: convergence of domain displacement error, r_u, with refinement and bandwidth, 30° Model.

would converge at a rate of 2 (as shown by the triangular convergence rate indicator on Figures 10, 11 and 12). However, in the material point method additional errors are introduced through non Gauss quadrature positioning of material points, partially filled elements and projection inaccuracies between the material points and the background grid [45]. Therefore we expect the convergence rate

This article is protected by copyright. All rights reserved.

Accepted Article

Accepted Article

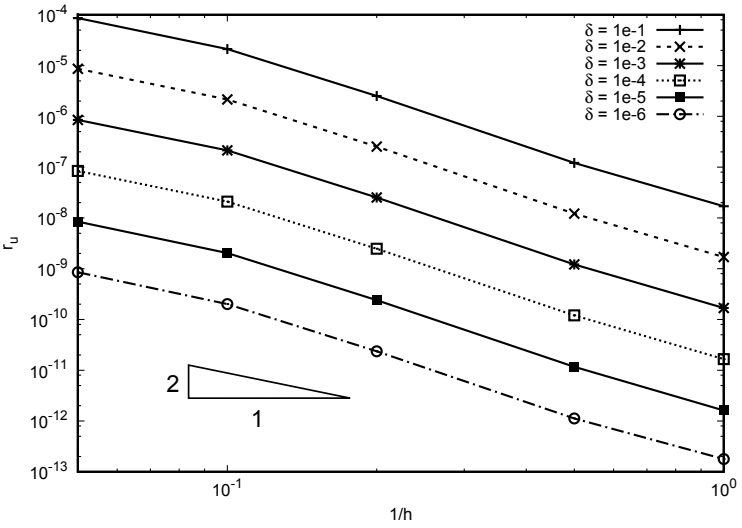

Figure 11. Compression of a contained block: convergence of domain displacement error, r_u, with refinement and bandwidth, δ, 45° Model.

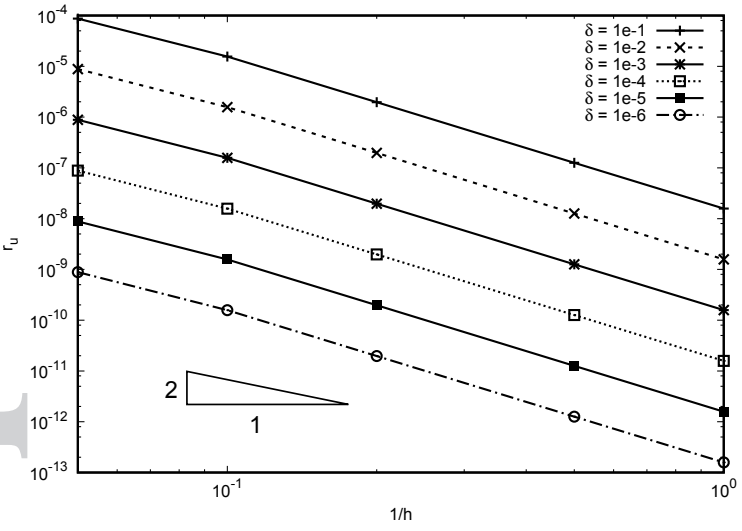

Figure 12. Compression of a contained block: convergence of domain displacement error, r_u, with refinement and bandwidth, 90° Model

of the material point method to be bounded by that of the underlying finite element basis. All models show similar uniform rates of convergence for displacement error showing errors decreasing with h-refinement, illustrating that the solution is unaffected by the presence of the IBs. As δ becomes smaller, the condition number of the global stiffness matrix should increase due to the increasing penalty contributions from $[K_2]$ and $[K_3]$ however these plots indicate that this does not seem to affect convergence for the investigated range of δ. Small variations in the convergence rates can be observed, particularly at the coarser discretisations, however these reduce as the simulations are refined and can be attributed to inaccuracies in the integration of the material stiffness due to

This article is protected by copyright. All rights reserved.

partially filled background elements. In particular, note that these variations are not observed in the 90° model in this case the elements are fully populated by material point domains.

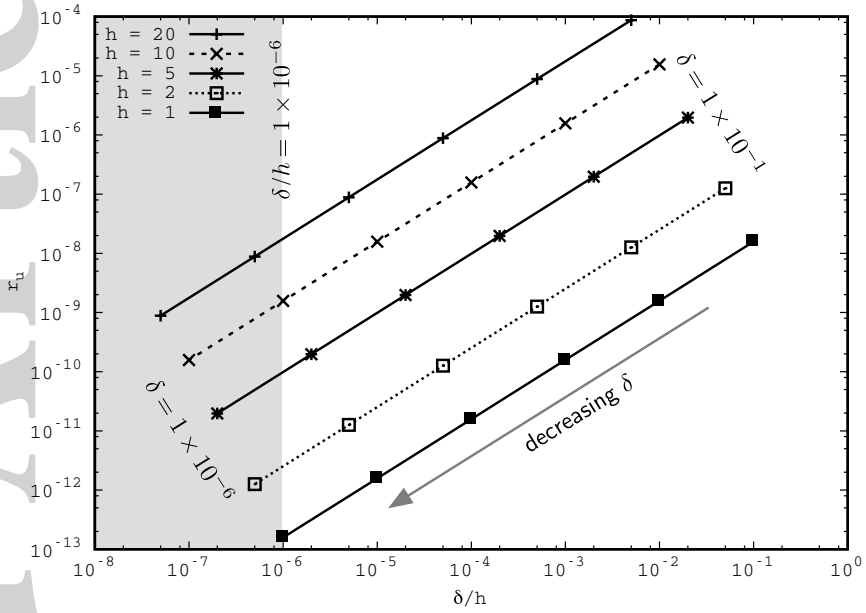

Figure 13. Compression of a contained block: displacement error, r_u, versus bandwidth/element size ratio for different background grid sizes.

Figure 13 shows the convergence for the 90 degree problem as a function of the ratio of the bandwidth to the element size, δ/h. As expected, decreasing δ/h decreases the error in the simulation and for $\delta/h \leq 1 \times 10^{-6}$ (the grey region in Figure 13) the maximum observed error is around 1×10^{-8}. The remainder of the numerical examples presented in this paper adopt a bandwidth size of $\delta = 1 \times 10^{-6} h$.

5.2. A deep beam under self-weight

The second example is a deep beam acting as a cantilever loaded with body force (see Figure 14) and demonstrates the influence on integration errors in the MPM when using the IB method. The problem domain is 100 mm square with full fixity at the left hand support implemented using the IB method. A body force of 1N/mm^2 is applied in a single step. Two convergence studies are conducted: firstly with respect to the number of material points in each grid element (keeping the element number constant) and secondly with respect to the number of grid elements, with material points per element kept constant. The background grid in the first study comprises a mesh of 10×10 mm elements, and since no analytical solution is available (as the support is full-fixity throughout) the MPM solution is compared with a FE solution using the same mesh, a suitable Gauss quadrature rule and standard imposition of essential boundary conditions, the goal being to demonstrate that the MPM approach with IBs converges to the standard FE solution for the same discretisation.

This article is protected by copyright. All rights reserved.

Accepted Article

The IB bandwidth used throughout this study $\delta = 1 \times 10^{-6} h$. The accuracy of the MPM model is assessed by a point-wise r_u on the y-displacement measured at point A in Figure 14 and results are presented in Table II, and a convergence plot in Figure 15a. As discussed in the previous section, the convergence rate of the MPM is governed by the underlying finite element basis. However, the convergence rate of the method can be reduced through inaccurate integration and projection between the material points and the background grid. In this example the MPM results are being compared with FEM on the same computational grid we are therefore investigating the error caused by inaccurate integration due to non-optimum material point locations.

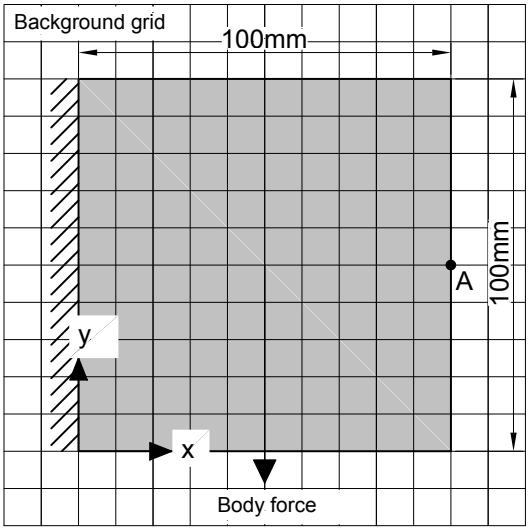

Figure 14. Deep beam with self-weight: problem layout.

In the second study the number of material points per element is kept constant at 16, and the grid is refined, and the results are compared with those from standard finite element analysis with the same mesh. Table III gives the same point-wise r_u on the y-displacement measured at point A in Figure 14 and the convergence is plotted in Figure 15b. Both of these studies demonstrate that the convergence of the material point method (reducing the errors associated with non-optimum quadrature locations) is not significantly influenced by the method of imposing the essential boundary conditions. Increasing the number of material points per element or reducing the size of the background grid cells both reduces the discrepancy between the MPM and FE results.

5.3. Simple shear

The third problem presented also investigates integration errors in the MPM with IBs but concentrating on partially-filled elements. In this example we consider a 100×100 mm under simple shear conditions. The problem is shown in Figure 16 where two 100×100 mm grid elements contain the domain discretised using 20×20 material points. The domain has a fully fixed essential

This article is protected by copyright. All rights reserved.

No. of material points per grid element	Normalised y-displacement error at A
3^2	1.6653×10^{-3}
5^2	5.9450×10^{-4}
10^2	1.4812×10^{-4}
15^2	6.5788×10^{-5}
20^2	3.6998×10^{-5}
25^2	2.3676×10^{-5}
40^2	1.0277×10^{-5}

Table II. Deep beam with self-weight: normalised y-displacement error at A with number of material points.

Number of background grid elements and finite elements	No. of d.o.f. (MPM & FE)	Normalised error
100 (h=10mm)	242	9.313×10^{-4}
400 (h=5mm)	882	3.110×10^{-4}
2500 (h=2mm)	520	7.558×10^{-5}
10000 (h=1mm)	20402	2.670×10^{-5}

Table III. Deep beam with self-weight: normalised y-displacement error at A compared to an equivalent FE model with h-refinement.

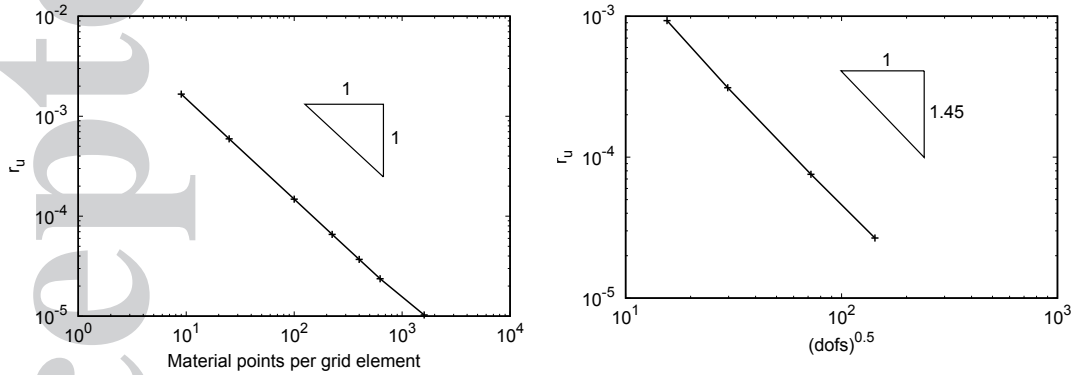

(a) Displacement error convergence with number of material points.

(b) Displacement error convergence with h-refinement of background grid.

Figure 15. Deep beam under self-weight: domain displacement error convergence.

boundary (using the IB method) on the left hand side and is shifted from $x = 0$ mm to $x = 100$ mm using the coordinate system shown. A shearing displacement of 10mm is imposed on the free end of the cantilever in a single step, while the top and bottom surfaces are fixed in the horizontal direction ($u_x = 0$) and allowed to move in the vertical direction only to achieve simple shear conditions.

In a simple shear problem, only uniform shear stresses (σ_{xy}) exists, and the analytical solution can be expressed as $\sigma_{xy} = \frac{E}{1+\nu}\varepsilon_{xy}$, where ε_{xy} is the prescribed shear strain (the sheared distance over

This article is protected by copyright. All rights reserved.

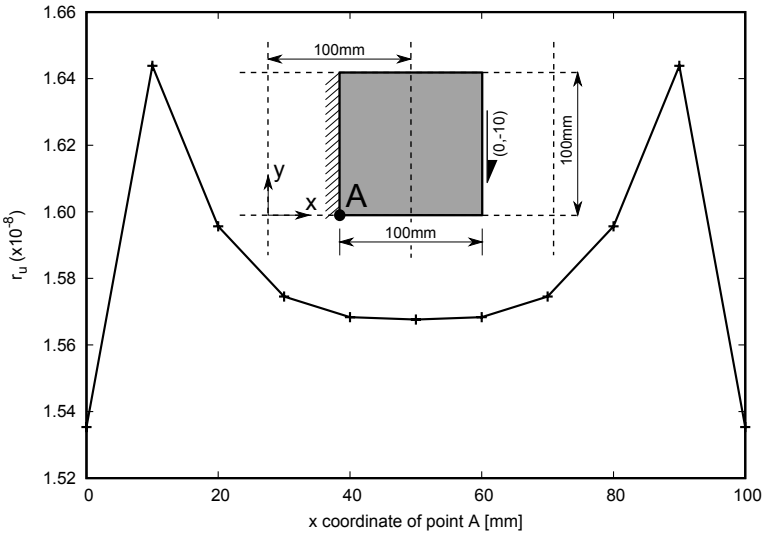

Figure 16. Simple shear: problem layout and $r_{\sigma_{xy}}$ error with location of essential boundary.

the length of the body). The shear stress error r_u is plotted with respect to the IB position (Figure 16). From the plot it is clear that the IB method leads to successful enforcement of an essential boundary condition almost anywhere within a grid element. Only when the implicit boundary moves very close to the edge of the grid element does accuracy drop however, it should be acknowledged that in all cases the error very small, being less than 2×10^{-8}, and any changes are relative to these very small numbers.

As expected the lowest error is observed when the domain is contained within a single element ($x_\mathsf{A} = 0$ or 100mm). As the domain moves between the two elements the error initially increases due to the poor integration of the element with containing few material points clustered at one edge (the right hand element in the figure). The error reduces with increasing translation and reaches a local minimum at $x_\mathsf{A} = 50$mm (half the domain in the two elements) before increasing again due to the problem's symmetry. The reduction in error between $x_\mathsf{A} = 10$mm and $x_\mathsf{A} = 50$mm is due to the improved integration of the right hand element as material points fill more of the element. The rate of improvement reduces with translation due to the increased level of error in the left hand element as material points move across the boundary between the two elements.

5.4. A slender cantilever beam

We now consider a a slender cantilever beam of dimensions 20×100 mm. The cantilever is oriented at three different angles, 0°, 45° and 90°, as shown in Figure 17 but the loading and geometry are effectively identical; only the discretisation changes. All models are fully fixed at one end using the IB method and are subjected to an incremental body force applied in the y-directions shown in Figure 17. A background MPM grid, having 2×2 mm elements is used, while the cantilever

This article is protected by copyright. All rights reserved.

Accepted Article

domain itself is discretised using 100 material points in every grid element. Note that we adopt a large number of material points per element to reduce the cell-crossing instability inherent in the MPM.

Displacement at the origin (the free end) is plotted against total body force for the three models in Figure 18. While the difference between the 0° and 90° cantilever model is negligible, the difference is more significant between 0° or 90°, and 45° cantilever models. This is likely due to poor numerical approximation where grid elements lack sufficient material points, or where material points are concentrated in a region of the element. As before, h-refinement of the background grid can be used to reduce this error. The percentage point-wise error between the 45° and 90° model is computed and plotted against the cantilever depth d normalised by the grid size h. The respective deflected shapes of both models using the finest background grid are shown in Figure 20 when the full body force is applied. To further demonstrate the quality of results obtained, stress contour plots for the 90° case at full body force are shown in Figure 21 on the undistorted configuration close to the support. The stresses are reported for a body force of 0.2N/mm^2 with a grid size of $1 \times 1\text{mm}$ and 25 material points per background grid cell in the original configuration. The problem is one where the only major gradients in stresses occur at the fully-fixed end, at the top and bottom of the section, and it can be seen that these concentrations are produced faithfully using the method.

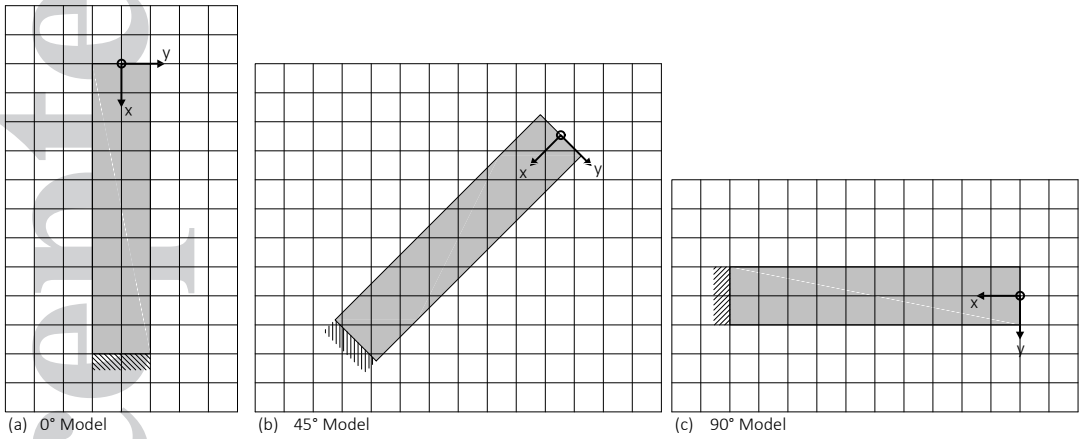

Figure 17. Cantilever Models (a) 0° Model; (b) 45° Model; (c) 90° Model.

5.5. *Rigid footing penetration*

The penultimate numerical example is a demonstration problem of the penetration of a rough rigid footing into an elastic domain, as shown in Figure 22. The elastic domain was 3×3m and the background grid had an element size of $h = 0.2\text{m}$. Each element initially contained 4 material points, as shown in Figure 22 (b). The bandwidth for the IBM method for all of the boundaries was set to $\delta = 1 \times 10^{-6}h$. A displacement of 1m was applied over 20 loadsteps and Figure 22 (c)

This article is protected by copyright. All rights reserved.

Accepted Article

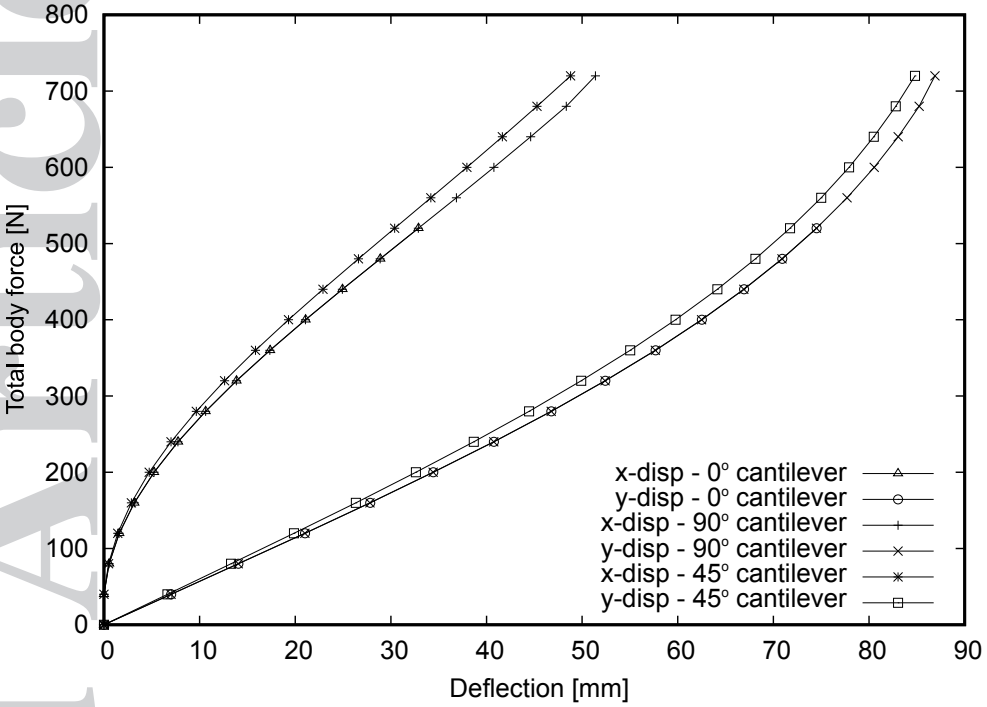

Figure 18. Cantilever: load-displacement for 0°, 45° and 90° models.

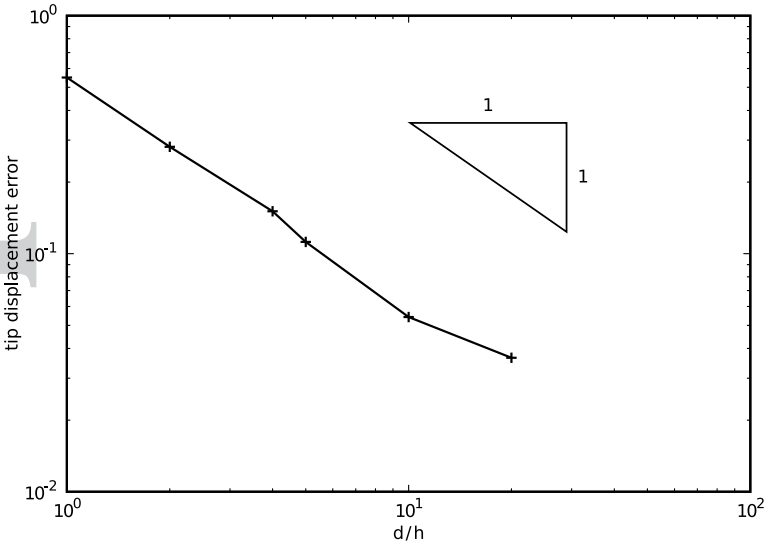

Figure 19. Cantilever: background grid h-refinement convergence between the 45° and 90° models.

through (f) shows the displaced material point profiles for loadsteps 2, 10 15 and 20. The material points are coloured according to their vertical displacement relative to their original position. The problem demonstrates the ability of the method to model a moving displacement boundary condition that does not coincide with the background grid.

This article is protected by copyright. All rights reserved.

Accepted Article

Accepted Article

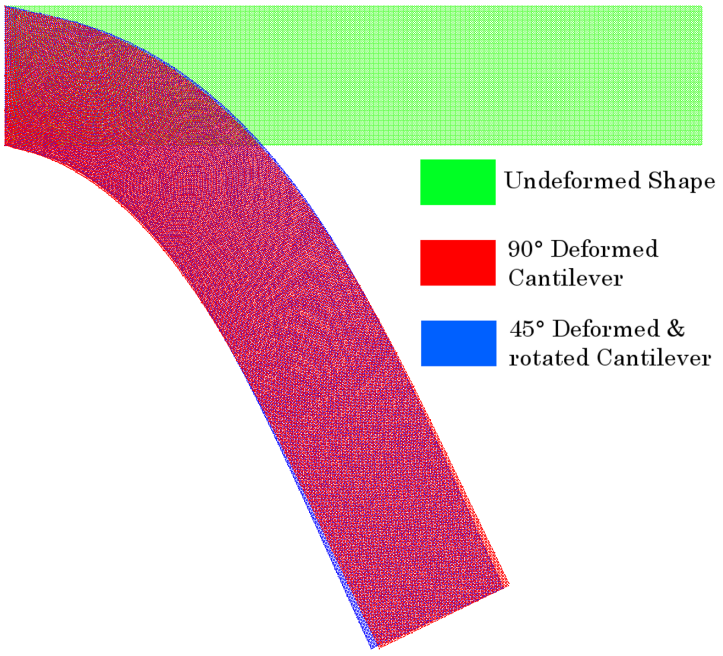

Figure 20. Cantilever: comparisons of deflections for 45° and 90° models.

5.6. Funnel penetration

The final numerical example is that of an elastic domain being forced through a curved funnel and is intended to demonstrate the use of the method for problems that cannot be rotated such that the boundaries coincide with the background grid. The problem geometry is shown in Figure 23 (a) where the roller boundary conditions on both the top and bottom boundaries and the prescribed displacement on the right edge were enforced using the IB method. A 4mm by 4mm background grid was used to solve the problem with four material points per background cell in the original configuration, as shown in Figure 23 (b) where the size of the points are determined by the material point volume. The elastic body, with the same material parameters as in the previous sections, was forced through the funnel with an incremental displacement of 4mm per loadstep. The bandwidth for the IBM method for all of the boundaries was set to $\delta = 1 \times 10^{-6} h$ and the curved boundary was approximated by piecewise linear segments over each background grid cell.

The deformation of the material points for the six loadsteps is shown in Figures 23 (c) through (h). The material points have been coloured according to their x-displacement measured from their initial positions, where the blue points have moved the greatest distance. Despite the very large displacement increment (three times the grid spacing) in each loadstep, as new material points move towards the inclined boundary condition their displacement trajectories align with the boundary. All of the material points remaining on the correct side of the inclined boundary condition throughout the simulation. The reduction in the domain height causes a region, coloured in red in Figures 23 (c)

This article is protected by copyright. All rights reserved.

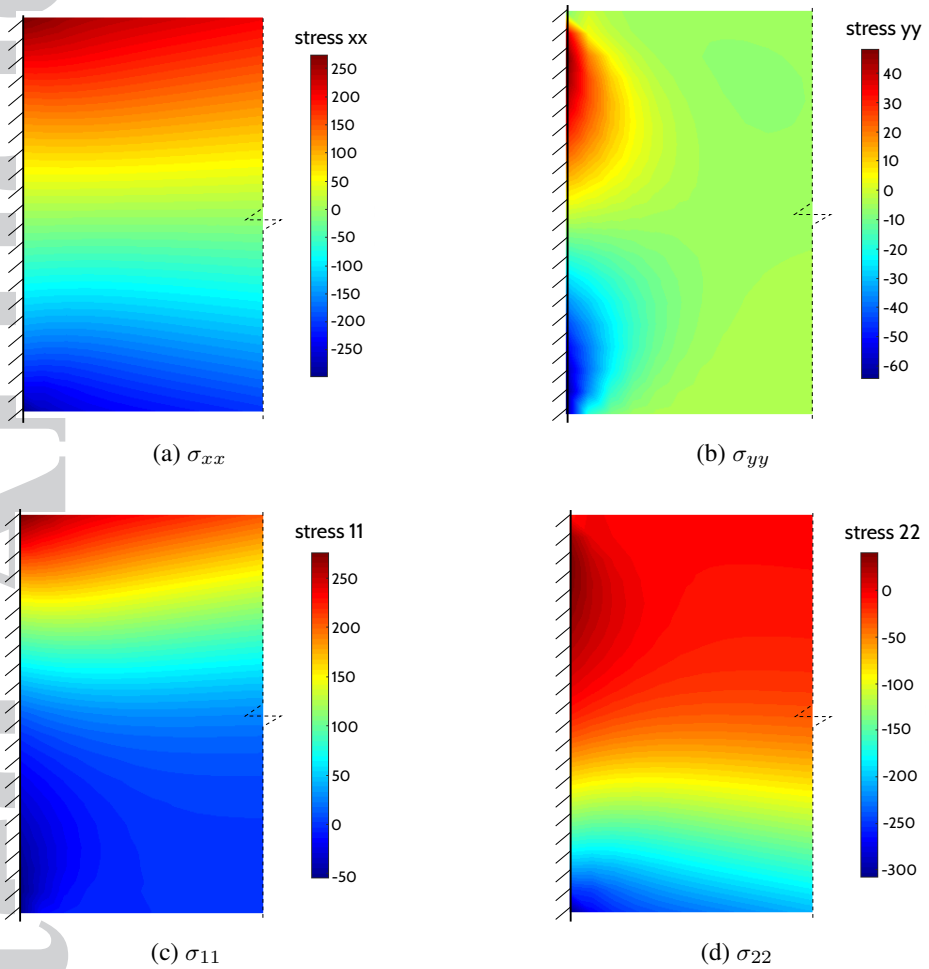

(a) σ_{xx} (b) σ_{yy}

(c) σ_{11} (d) σ_{22}

Figure 21. Cantilever: stress contour plots close to the fixed end (all stresses in MPa).

through (h), of reduced x-displacement whilst a region towards the top of the problem, coloured in blue, increases in displacement. The right hand boundary remains vertical with a uniform value of displacement irrespective of its position within the background grid.

6. CONCLUSIONS

The material point method provides a means of analysing problems in solid mechanics for which conventional finite elements, and other numerical techniques, struggle, notably those involving very large deformations. Since problem domain boundaries do not necessarily coincide with the boundary of the grid on which material point method calculations are carried out, an issue arises when wishing to model non-zero essential boundary conditions and roller boundary type conditions on a regular background grid. In this paper, we have presented a simple technique, similar to a more limited version previously applied to finite elements, and shown how it can be adapted to

This article is protected by copyright. All rights reserved.

Accepted Article

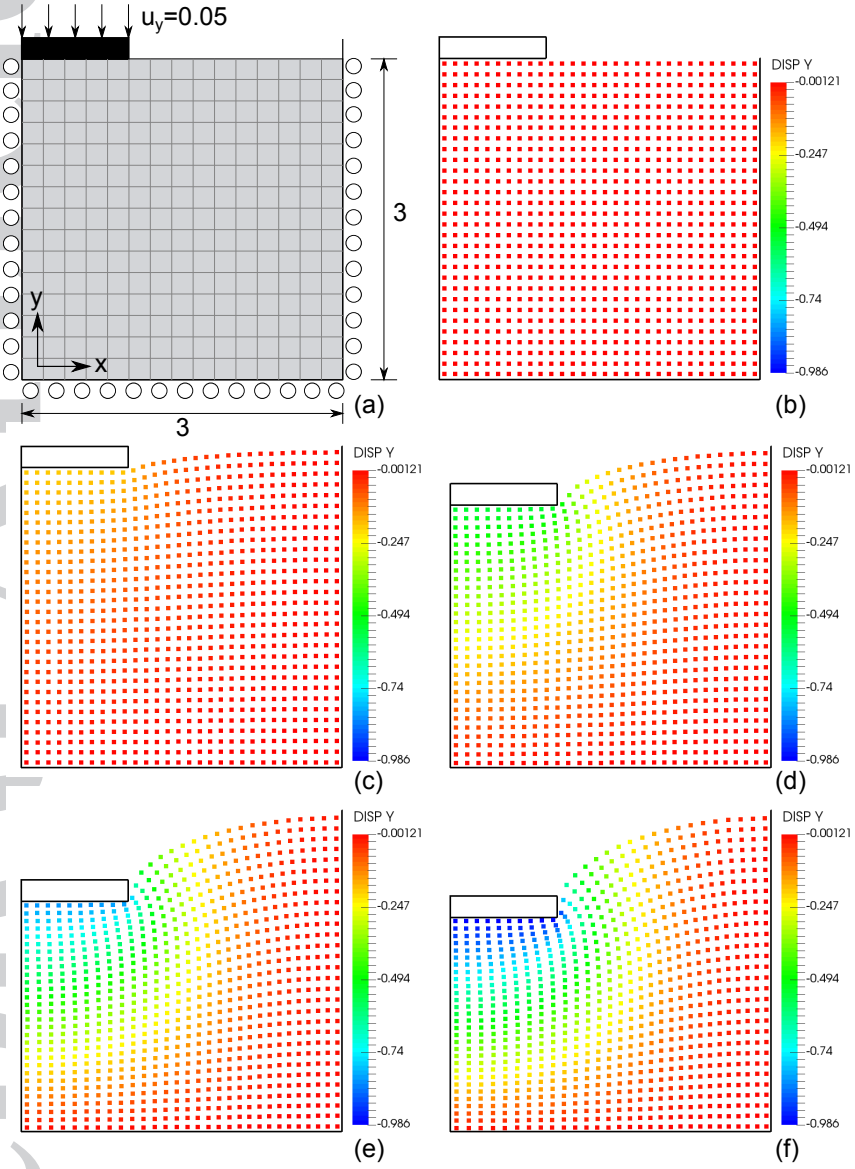

Figure 22. Rigid footing penetrating into an elastic domain: (a) problem definition, (b) material point discretisation and (c) through (f) material point deformation with increasing vertical displacement coloured according to the vertical displacement.

model inclined boundaries and then demonstrated its use on problems analysed using the implicit material point method. To the authors' knowledge this is the first time that a general method has been proposed that allows arbitrary inhomogeneous Dirichlet boundary conditions (zero and non-zero values at any inclination) to be imposed in the MPM. In particular the method presented in this paper is different from other approaches in the MPM in that: (i) the boundaries are independent of the background mesh [26], (ii) it does not require artificially stiff regions of material points to be introduced [25] and (iii) the method does not rely on spurious *mirroring* of the problem domain to imposed symmetry as seen in other MPM approaches [11]. The method significantly extends the

This article is protected by copyright. All rights reserved.

Accepted Article

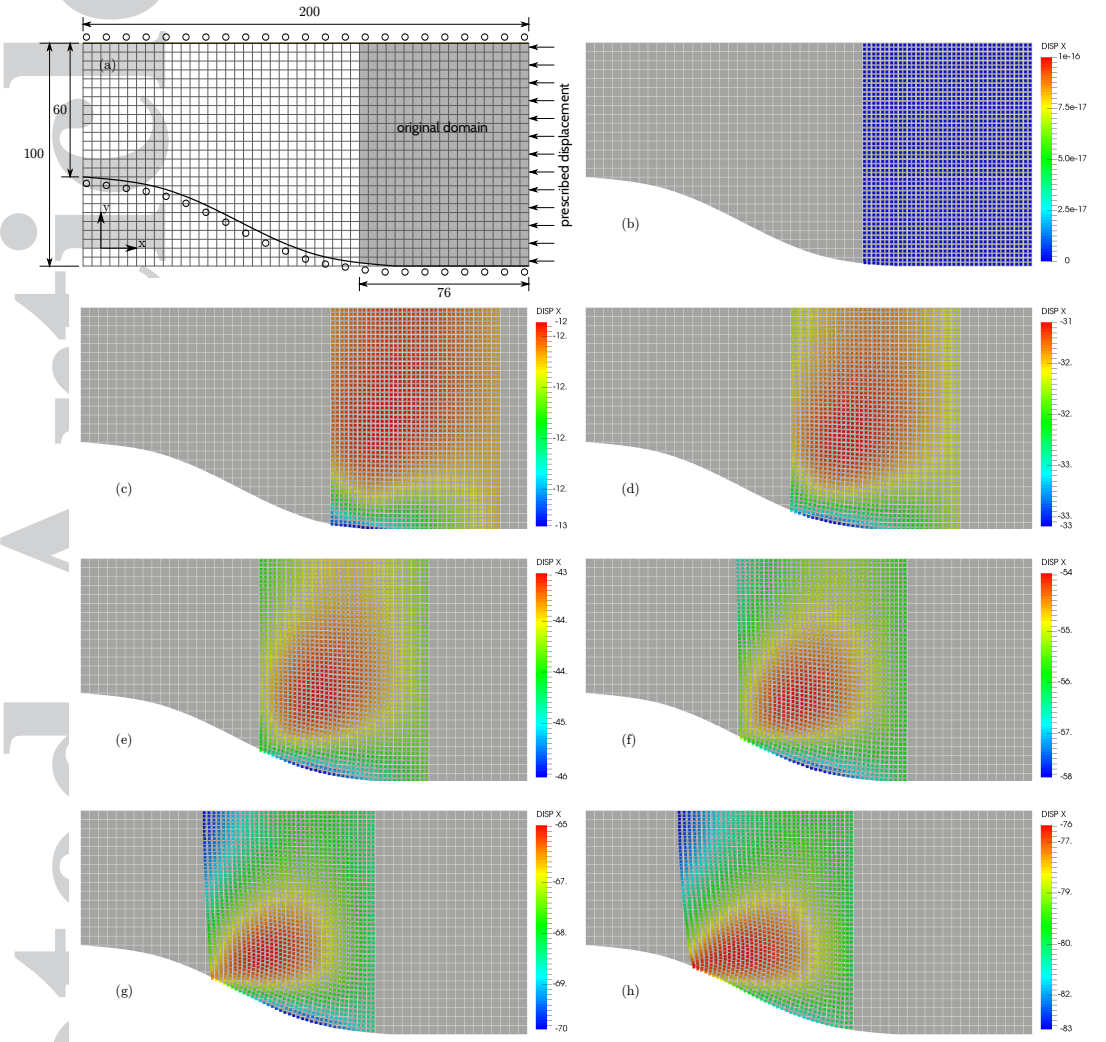

Figure 23. Movement of an elastic domain through a curved constriction: (a) problem dimensions, (b) initial MP discretisation and (c) through (h) deformed material point positions coloured according to their x-displacement.

applicability of the MPM to examine problems that were previously unassailable using the method, the work itself is simple to extend to 3D, and the inclined boundary method can equally be applied to standard finite elements.

An extension to this work would be to combine the IBC method with traction boundary conditions and thereby allowing any type of boundary condition to be modelled within the material point method. The work could also be extended to allow for frictional boundary conditions (limiting shear traction dependent on the normal pressure) that would provide a more realistic interface for soil-structure interaction problems.

ACKNOWLEDGEMENT

This article is protected by copyright. All rights reserved.

The work presented in this paper is part of a study of seabed ploughing for offshore energy infrastructure and is funded by Grants EP/M000397/1 and EP/M000362/1 of the UK EPSRC.

REFERENCES

1. Belytschko T, Lu YY, Gu L. Element-free Galerkin methods. *International Journal for Numerical Methods in Engineering* 1994; **37**:229–256.
2. Belytschko T, Krongauz Y, Organ D, Fleming M, Krysl P. Meshless methods: An overview and recent developments. *Computer Methods in Applied Mechanics and Engineering* 1996; **139**(1-4):3 – 47.
3. Nguyen VP, Rabczuk T, Bordas S, Duflot M. Meshless methods: A review and computer implementation aspects. *Mathematics and Computers in Simulation* 2008; **79**(3):763 – 813.
4. Tian Y, Cassidy MJ, Randolph MF, Wang D, Gaudin C. A simple implementation of ritss and its application in large deformation analysis. *Computers and Geotechnics* 2014; **56**:160–167.
5. O'Sullivan C. *Particulate Discrete Element Modelling: A Geomechanics Perspective*. CRC Press, 2011.
6. Liu G, Liu M. *Smoothed Particle Hydrodynamics: A Meshfree Particle Method*. World Scientific, 2003.
7. Sulsky D, Chen Z, Schreyer H. A particle method for history-dependent materials. *Computer Methods in Applied Mechanics and Engineering* 1994; **118**:179–196.
8. Guilkey J, Weiss J. Implicit time integration for the material point method: Quantitative and algorithmic comparisons with the finite element method. *International Journal for Numerical Methods in Engineering* 2003; **57**:1323–1338.
9. Belytschko T, Liu WK, Moran B, Elkhodary K. *Nonlinear Finite Elements for Continua and Structures, 2nd Edition*. Wiley, 2013.
10. Bardenhagen S, Kober E. The generalized interpolation material point method. *CMES- Computer Modeling in Engineering and Sciences* JUN 2004; **5**(6):477–495.
11. Sadeghirad A, Brannon RM, Burghardt J. A convected particle domain interpolation technique to extend applicability of the material point method for problems involving massive deformations. *International Journal for Numerical Methods in Engineering* 2011; **86**(12):1435–1456.
12. Sadeghirad A, Brannon R, Guilkey J. Second-order convected particle domain interpolation (CPDI2) with enrichment for weak discontinuities at material interfaces. *International Journal for Numerical Methods in Engineering* 2013; **95**:928952.
13. Andersen S, Andersen L. Modelling of landslides with the material-point method. *Computational Geosciences* 2010; **14**:137–147.
14. Soga K, Alonso E, Yerro A, Kumar K, Bandara S. Trends in large-deformation analysis of landslide mass movements with particular emphasis on the material point method. *Géotechnique* 2016; **66**(3):248–273.
15. Jassim I, Stolle D, Vermeer P. Two-phase dynamic analysis by material point method. *International Journal for Numerical and Analytical Methods in Geomechanics* 2013; **37**(15):2502–2522.
16. Yang P, Gan Y, Zhang X, Chen Z, Qi W, Liu P. Improved decohesion modeling with the material point method for simulating crack evolution. *International Journal of Fracture* 2014; **186**(1):177–184.
17. Ma S, Zhang X, Qiu X. Comparison study of mpm and sph in modeling hypervelocity impact problems. *International Journal of Impact Engineering* 2009; **36**(2):272 – 282.
18. Liu Y, Qiu X, Zhang X, Yu T. Response of woodpecker's head during pecking process simulated by material point method. *PLoS ONE* 2015; **10(4)**.
19. Fernández-Méndez S, Huerta A. Imposing essential boundary conditions in mesh-free methods. *Computer Methods in Applied Mechanics and Engineering* 2004; **193**:1257–1275.
20. Augarde CE, Deeks AJ. On the effects of nodal distributions for imposition of essential boundary conditions in the MLPG meshfree method. *Communications in Numerical Methods in Engineering* 2005; **21**:389–395.

This article is protected by copyright. All rights reserved.

Accepted Article

21. Kumar AV, Burla R, Padmanabhan S, Gu L. Finite element analysis using nonconforming mesh. *Journal of Computing and Information Science in Engineering* Aug 2008; **8**(3):031 005–(1–11).
22. Lauder KD, Brown MJ, Bransby MF, Boyes S. The influence of incorporating a forecutter on the performance of offshore pipeline ploughs. *Applied Ocean Research* 2013; **39**:121 – 130.
23. Charlton TJ, Coombs WM, Augarde CE. On the implicit implementation of the Generalised Interpolation Material Point method. *Proc. 23rd ACME conference (Gil & Sevila, Eds), Swansea, April.*, 2015.
24. Charlton TJ, Coombs WM, Augarde CE. IGIMP: the implicit Generalised Interpolation Material Point method. *International Journal for Numerical Methods in Engineering* Under review; .
25. Sołowski WT, Sloan SW. Evaluation of material point method for use in geotechnics. *International Journal for Numerical and Analytical Methods in Geomechanics* 2015; **39**(7):685–701.
26. Phuong N, van Tol A, Elkadi A, Rohe A. Numerical investigation of pile installation effects in sand using material point method. *Computers and Geotechnics* 2016; **73**:58 – 71.
27. Wieckowski Z. The material point method in large strain engineering problems. *Computer Methods in Applied Mechanics and Engineering* 2004; **193**(3941):4417 – 4438. The Arbitrary Lagrangian-Eulerian Formulation.
28. Beuth L, Wieckowski Z, Vermeer PA. Solution of quasi-static large-strain problems by the material point method. *International Journal for Numerical and Analytical Methods in Geomechanics* 2011; **35**(13):1451–1465.
29. Freytag M, Shapiro V, Tsukanov I. Finite element analysis in situ. *Finite Elements in Analysis and Design* 2011; **47**(9):957 – 972.
30. Schillinger D, Ruess M, Zander N, Bazilevs Y, Düster A, Rank E. Small and large deformation analysis with the p- and b-spline versions of the finite cell method. *Computational Mechanics* 2012; **50**(4):445–478.
31. Hautefeuille M, Annavarapu C, Dolbow JE. Robust imposition of dirichlet boundary conditions on embedded surfaces. *International Journal for Numerical Methods in Engineering* 2012; **90**(1):40–64.
32. Ramos A, Aragn A, Soghrati S, Geubelle P, Molinari JF. A new formulation for imposing Dirichlet boundary conditions on non-matching meshes. *International Journal for Numerical Methods in Engineering* 2015; **103**(6):430–444.
33. Burla R. Finite element analysis using uniform b-spline approximation and implicit boundary method. Phd thesis, University of Florida 2008.
34. Kumar AV, Padmanabhan S, Burla R. Implicit boundary method for finite element analysis using non-conforming mesh or grid. *International Journal for Numerical Methods in Engineering* 2008; **74**(9):1421–1447.
35. Burla RK, Kumar AV. Implicit boundary method for analysis using uniform b-spline basis and structured grid. *International Journal for Numerical Methods in Engineering* 2008; **76**(13):1993–2028.
36. Kantorovich L, Krylov V. *Approximate Methods of Higher Analysis*. Interscience Publishers, 1958.
37. Höllig K, Reif U, Wipper J. Weighted extended b-spline approximation of dirichlet problems. *SIAM Journal on Numerical Analysis* 2001; **39**(2):442–462.
38. Höllig K, Reif U. Nonuniform web-splines. *Computer Aided Geometric Design* 2003; **20**(5):277 – 294.
39. Höllig K, Apprich C, Streit A. Introduction to the web-method and its applications. *Advances in Computational Mathematics* 2005; **23**(1):215–237.
40. Zhang W, Zhao L. Exact imposition of inhomogeneous dirichlet boundary conditions based on weighted finite cell method and level-set function. *Computer Methods in Applied Mechanics and Engineering* 2016; **307**:316 – 338.
41. Rvachev V, Sheiko T, Shapiro V, Tsukanov I. Transfinite interpolation over implicitly defined sets. *Computer Aided Geometric Design* 2001; **18**(3):195 – 220.
42. Belytschko T, Gracie R, Ventura G. A review of extended/generalized finite element methods for material modeling. *Modelling and Simulation in Materials Science and Engineering* 2009; **17**(4):043 001.
43. Yazid A, Abdelkader N, Abdelmadjid H. A state-of-the-art review of the x-fem for computational fracture mechanics. *Applied Mathematical Modelling* 2009; **33**(12):4269 – 4282.
44. Cortis M, Coombs WM, Augarde CE. Implicit essential boundaries in the Material Point Method. *Proc. 24th UK Conference of the Association for Computational Mechanics in Engineering. Cardiff, UK*, 2016; 116–119.

This article is protected by copyright. All rights reserved.

Accepted Article

45. Sulsky D, Gong M. Improving the material-point method. *Innovative Numerical Approaches for Multi-Field and Multi-Scale Problems*, *Lecture Notes in Applied and Computational Mechanics*, vol. 81, Weinberg K, Pandolfi A (eds.). Springer International Publishing, 2016; 217–240.

Accepted Article

This article is protected by copyright. All rights reserved.